Dependence of Plasma Parameters in Hydrogen Pellet Ablation Cloud on the Background Plasma Conditions*)

Motoshi GOTO[1,2], Hiroya UYAMA[3], Takuya OGAWA[4], Khanit MATRA[5], Gen MOTOJIMA[1,2], Tetsutarou OISHI[1,2] and Shigeru MORITA[1,2]

[1]*National Institute for Fusion Science, Toki 509-5292, Japan*
[2]*Department of Fusion Science, SOKENDAI (The Graduate University for Advanced Studies), Toki 509-5292, Japan*
[3]*National Institute of Technology, Toyama College, Toyama 939-8630, Japan*
[4]*Department of Electrical and Electronic Engineering, Utsunomiya University, Utsunomiya 321-8505, Japan*
[5]*Department of Electrical Engineering, Srinakharinwirot University, Ongkharak, Nakhonnayok, 26120, Thailand*

(Received 25 December 2018 / Accepted 28 January 2019)

UV-visible spectra of the radiation from hydrogen pellet ablation clouds have been measured in the Large Helical Device. The temporal development of the Balmer-α line intensity shows a peaked profile with FWHM (full width at half maximum) of approximately 150 μs. The electron temperature T_e, electron density n_e, and plasma volume V are evaluated by fitting of the measured spectra with a complete LTE (local thermodynamic equilibrium) model. The results shows that T_e is almost unchanged, while n_e and V increases and decreases monotonically, respectively, in the dominant time period around the intensity peak. The same analyses made for several different magnetic configurations have revealed that n_e has a tendency to become higher when the magnetic field strength is higher, while no clear dependence on the magnetic axis position has been observed. On the other hand, T_e shows little dependence either on the magnetic field strength or the magnetic axis position.

Keywords: hydrogen pellet injection, ablation cloud, Stark broadening, radiative recombination continuum, radiative attachment continuum, complete LTE

DOI: 10.1585/pfr.14.3402053

1. Introduction

The hydrogen pellet injection is considered to be an essential method for the particle fueling of fusion plasma [1]. Understanding the characteristics of the pellet ablation mechanism is indispensable for optimizing the fueling efficiency.

The hydrogen pellet is surrounded by localized high density plasma, the so-called ablation cloud, immediately after plunging into the background plasma. The ablation cloud emits intense radiation which helps us obtain clues for revealing plasma states in the pellet ablation cloud. Emission lines of neutral hydrogen obviously exhibit the Stark broadening, from which the electron density n_e can be evaluated. The electron temperature T_e is inferred from the continuum radiation profiles and the discrete line intensities.

In our previous study [2], it has been verified that the complete LTE (local thermodynamic equilibrium) is approximately established in the ablation cloud. In that case, the entire Balmer-series spectrum including the discrete lines and the continuum is determined only by T_e and n_e aside from the absolute intensity. We have actually derived T_e and n_e from spectra measured in the Large Helical Device (LHD).

The parameters obtained in that study are representative values of the ablation cloud. The actual ablation cloud should have a spatial structure in it, and it is unclear whether the LTE is established in the entire region of the ablation cloud. Although some efforts have been made for a spatially resolved measurement inside the ablation cloud [3,4], no definitive conclusion has been obtained to date.

It is also unclear, and interesting, whether the derived representative parameters are the universal parameters irrespective of the background plasma conditions, i.e., the magnetic configuration and the magnetic field strength. In this study, we focus our interest on measuring representative T_e and n_e values for different magnetic configurations in LHD and on deriving dependence of T_e and n_e in the ablation cloud on the plasma condition.

2. Experimental Setup

The measurement has been made for discharges in LHD. Pellets are injected from the outboard side of the vacuum vessel on the equatorial plane [5]. The pellet has a cylindrical shape having the diameter and the length of

author's e-mail: goto@nifs.ac.jp

*) This article is based on the presentation at the 27th International Toki Conference (ITC27) & the 13th Asia Pacific Plasma Theory Conference (APPTC2018).

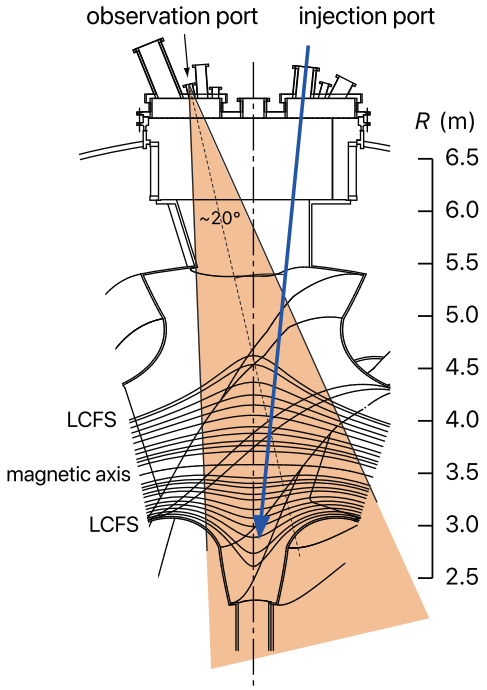

Fig. 1 Top view of LHD vacuum vessel around the pellet injection port. The pellet trajectory is drawn by the blue solid arrow, and the approximate field of view of the present observation is indicated by the area colored orange.

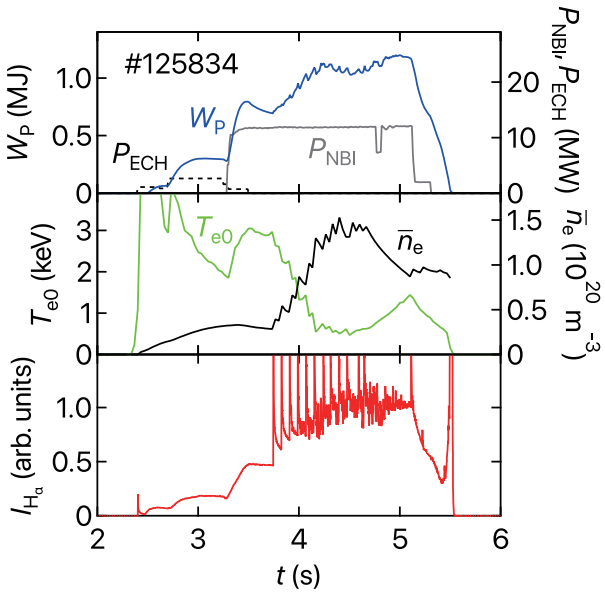

Fig. 2 Example of typical discharges for the present pellet injection experiment. The top panel shows the stored energy W_P, NBI power P_{NBI}, and ECH power P_{ECH}. The middle panel shows the central electron temperature T_{e0} and the line-averaged electron density $\bar{n}_e$, and the bottom panel shows the Balmer-α line intensity I_{H_α}.

roughly 3 mm. The number of atoms contained in a pellet is in the order of 10^{21}. The pellet is injected by a pneumatic pipe-gun type accelerator into the plasma with the velocity of approximately 1 km s^{-1}, which has been measured with a time-of-flight method.

Figure 1 shows the top view of the vacuum vessel where the pellet trajectory is indicated by the blue solid arrow.

An optical fiber end is placed at an observation port near the pellet injection port and observes the radiation from the ablation cloud. The approximate field-of-view, which is determined by the numerical aperture of the optical fiber of 0.2, is shown with the area colored orange in Fig. 1. It is confirmed that the ablation cloud always stays inside the field-of-view.

The light received by the optical fiber is transferred to a UV-visible spectrometer having a focal length of 50 cm (Chromex 500is). The spectrometer is equipped with a grating of 100 grooves/mm which gives the reciprocal linear dispersion of 19.984 nm/mm. The instrumental function is approximated with a Gaussian function having FWHM of 1.64 nm with the entrance slit width of 50 μm which is fixed throughout the present measurement. A CCD (charge coupled device) which has 1024 × 255 pixels with each pixel size being 26 × 26 μm^2 (Andor DU-420 V) is used for the detector. The sensitivity of the entire system has been absolutely calibrated with a standard lamp (Labsphere USS-600C).

The fast kinetic mode is used for recording high temporal resolution spectra, i.e., the horizontal direction with 1024 pixels is used for recording a spectrum and its temporal development is stored in the vertical direction. The time resolution is determined by the vertical charge shift speed of the CCD, which is 16 μs in the present case. The maximum observation time length is simply determined as 16 μs/pixel × 255 pixels = 4080 μs. Intense radiation from the ablation cloud lasts roughly 400 μs. Because the observable time period is rather short (∼ 4 ms), the CCD is given a trigger from the pellet injection system for synchronizing the data acquisition start with the pellet injection.

Figure 2 shows an example of the discharges for the hydrogen pellet injection experiment. The plasma is initiated by the electron cyclotron heating (ECH) and is sustained by the neutral beam injection (NBI). No gas fueling is made in this case, thus the plasma is made with the residual gas in the vacuum vessel.

Twelve pellets are sequentially injected between t = 3.5 s and t = 5 s in this case, which can be recognized by the Balmer-α line intensity signal I_{H_α} at the bottom panel in Fig. 2. It is also observed that the line-averaged electron density $\bar{n}_e$ and the central electron temperature T_{e0} increases and drops, respectively, by each pellet injection. While the number of pellets injected in a discharge is changed depending on the purpose of the experiment, the present observation always targets on the first pellet.

An example of the measured spectra is plotted with the red crosses in Fig. 3. This spectrum has been taken at t_{rel} = 80 μs, where t_{rel} is the time relative to the intensity

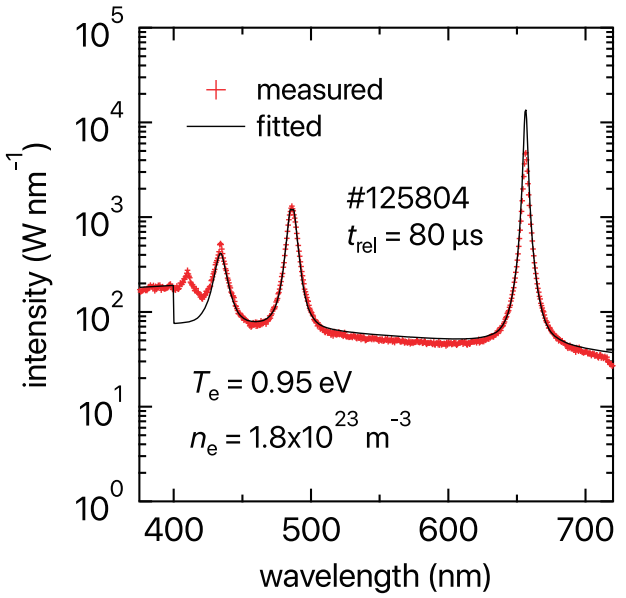

Fig. 3 An example of spectra measured in the present study (red crosses) and the fitted curve with the model spectrum (black solid lines). The T_e and n_e values are the result of the fitting.

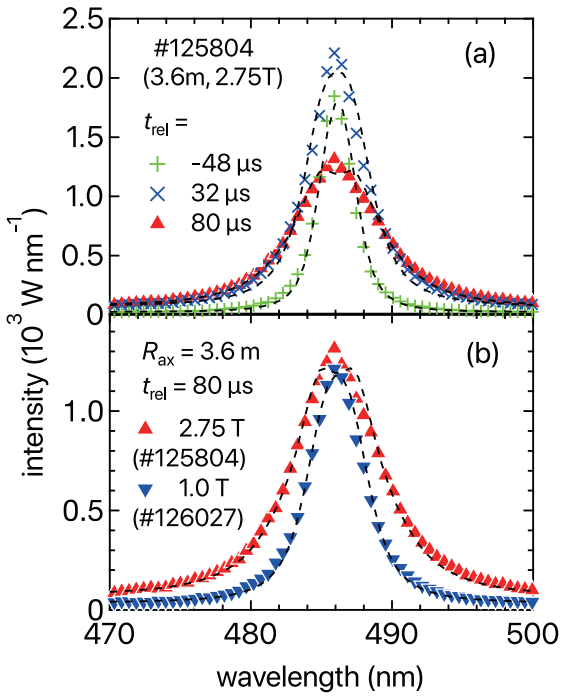

Fig. 4 Examples of the measured Balmer-β profiles at different observation timings (a) and for different magnetic field strengths (b). The black dashed lines show the fitted curves. The corresponding n_e values are 3.9×10^{22}, 9.6×10^{22}, and 1.8×10^{23} m^{-3} for $t_{rel} = -48$, 32, and 80 μs, respectively, in (a), and 1.8×10^{23} and 8.3×10^{22} m^{-3} for $B_{ax} = 2.75$ and 1 T, respectively, in (b).

peak of the Balmer-α line center as explained later. Four discrete lines, i.e., Balmer-α, β, γ, and δ, are observed, and all the discrete lines are found to be noticeably broadened.

Because the line profile observed for the pellet ablation cloud is known to be dominated by the Stark broadening effect [2], this result suggests that n_e can be evaluated through an analysis of the line profile. Moreover, it is found that the broadening width and thus n_e change with time as shown in Fig. 4 (a). It is also noticed that the line width, or n_e, is different even at the same observation timing when the magnetic field strength is changed as shown in Fig. 4 (b).

In the actual analysis, the measured spectra are fitted with a model spectrum which will be discussed in detail in the next section, and T_e, n_e, and the plasma volume V are derived.

3. LTE Spectrum

Under the complete LTE, the population of any level p, which includes the ground state, is expressed by the Saha-Boltzmann equation [6] as

$$n(p) = p^2 \left(\frac{h^2}{2\pi m k T_e}\right)^{3/2} \exp\left(\frac{R}{p^2 k T_e}\right) n_e n_i, \qquad (1)$$

where h, R, k, and m are the Plank constant, Rydberg constant, Boltzmann constant, and electron mass, respectively, and p and n_i are the principal quantum number of neutral hydrogen and the proton density, respectively. Although $n(p)$ is generally a function of T_e, n_e, and n_i, $n_i = n_e$ should be a reasonable assumption in the present case because pure hydrogen plasma is expected in the ablation cloud, and, consequently, $n(p)$ is determined only by T_e and n_e (or n_i).

The Balmer series lines of neutral hydrogen correspond to transitions from levels $p > 2$ to $p = 2$ level. The line profile of a transition from level p is here denoted as $\rho_p^{\rm line}(\lambda)$, where λ is the wavelength, and $\rho_p^{\rm line}(\lambda)$ is normalized as

$$\int \rho_p^{\rm line}(\lambda) {\rm d}\lambda = 1. \qquad (2)$$

In the present study, $\rho_p^{\rm line}(\lambda)$ is dominated by the Stark broadening and other broadening effects, such as the Doppler broadening, are negligible. The convolution of the Stark broadening and the instrumental function is evaluated when the synthetic line profile is compared with the measured profiles.

The database of Ref. [7] is adopted for calculating the Stark broadening profiles. Although the Stark broadening generally depends on n_e and T_e, the dependence on T_e is small. Thus $T_e = 1$ eV, which is the representative value found in the previous study [2], is used throughout.

The continuum radiation spectrum, which is also an essential part for constructing the entire spectrum, dominantly consists of two components, i.e., the radiations accompanying the radiative recombination and the radiative attachment processes. The radiative attachment is a pro-

cess in which a hydrogen atom turns into a negative hydrogen ion by capturing an electron. It is confirmed that the Bremsstrahlung is negligibly small in the plasma condition considered here.

The radiation power density spectrum due to the radiative recombination process to level p, $\rho_p^{\rm rec}(\lambda)$, is expressed as [6]

$$\rho_p^{\rm rec}(\lambda) = 2\sqrt{\frac{2}{\pi}}p^2\frac{h^4c^2}{m^{3/2}\lambda^5}\left(\frac{1}{kT_{\rm e}}\right)^{3/2}\sigma_p^{\rm ion}(\lambda) \times \exp\left(-\frac{hc/\lambda-\chi_p}{kT_{\rm e}}\right)n_{\rm e}n_{\rm i}, \quad (3)$$

where $\sigma_p^{\rm ion}(\lambda)$ is the cross section of the photoionization, which is the inverse process of the radiative recombination, and χ_p is the ionization potential of level p. The values of $\sigma_p^{\rm ion}(\lambda)$ are evaluated by the method in Ref. [8].

The radiation power density spectrum for the radiative attachment process is obtained in a similar manner to the case of the radiative recombination as

$$\rho^{\rm att}(\lambda) = \sqrt{\frac{2}{\pi}}\frac{h^4c^2}{m^{3/2}\lambda^5}\left(\frac{1}{kT_{\rm e}}\right)^{3/2}\sigma^{\rm det}(\lambda) \times \exp\left(-\frac{hc/\lambda-\chi_{\rm H^-}}{kT_{\rm e}}\right)n_{\rm e}n_0, \quad (4)$$

where $\sigma^{\rm det}(\lambda)$ is the cross section of the photodetachment, which is the inverse process of the radiative attachment, $\chi_{\rm H^-}$ is the detachment potential of the negative ion, and n_0 is the ground state atom density. The values of $\sigma^{\rm det}(\lambda)$ are taken from Ref. [9].

The entire spectrum $\rho(\lambda)$ is obtained as a superposition of all the components discussed above as

$$\rho(\lambda) = \sum_p n(p)\rho_p^{\rm line}(\lambda) + \rho^{\rm rec}(\lambda) + \rho^{\rm att}(\lambda). \quad (5)$$

What we obtain in the measurement is the radiation power integrated over the radiation volume in the ablation cloud. Here, a homogeneous plasma having the volume V is assumed and $P(\lambda) = \rho(\lambda)V$ is used for fitting the measured spectra. It is finally emphasized that $P(\lambda)$ is determined only by $T_{\rm e}$, $n_{\rm e}$, and V under the complete LTE, which is assumed throughout the present study. More specifically, $n_{\rm e}$ is dominantly determined by the Stark broadening width of discrete lines, and $T_{\rm e}$ is mainly derived by the spectral profile of the continuum radiation and the continuum radiation intensity relative to that of the discrete lines.

Figure 3 shows the fitted curve of the measured spectrum with the black solid line as an example. The Balmer-δ line is completely omitted in the analysis because the present $n_{\rm e}$ values are close to the Inglis-Teller limit [10] and are sometimes out of range of the Stark broadening database used here. The central part of the Balmer-α line is also excluded from the wavelength range used for the fitting because this line is known to be often affected by the self-reabsorption effect [2].

The maximum wavelength of the radiative recombination continuum corresponds to the ionization potential of the $p = 2$ level, which is translated into the wavelength of ~ 364.7 nm. In high density plasmas, however, due to the ionization limit lowering effect, the continuum radiation spectrum continuously extends beyond that maximum wavelength. It is known that the extended part of the spectrum is expressed by the same equation as Eq. (3) but with $\sigma_p^{\rm ion}(\lambda)$ evaluated with the bound-bound Gaunt factor [6]. In the present analysis, calculation of the radiative recombination continuum spectrum is extended up to 400 nm.

The fitted curves for the measured Balmer-β line profiles in Fig. 4 are also shown with the black dashed lines in the same figure as another example of the fitting. It is confirmed that the measure line profiles are well explained by the Stark broadening.

4. Results and Discussion

The measurement was first made for two groups of discharges for which $R_{\rm ax}$ is fixed at 3.6 m but the magnetic field strength is different. One group consists of 14 discharges with $B_{\rm ax} = 2.75$ T and the other is made up of 5 discharges with $B_{\rm ax} = 1$ T. Although $R_{\rm ax}$ of the second group is actually changed from 3.53 m to 3.6 m shot by shot, they are treated as a single group labeled as $R_{\rm ax} = 3.6$ m (1 T). When more than one pellet is injected in a single discharge, the first pellet is always the observation target as mentioned above.

Figure 5 (a) shows the temporal development of the intensity at the line center of the Balmer-α, $I_{\rm H_\alpha}(0)$, taken from the measured spectra for $R_{\rm ax} = 3.6$ m (red) and $R_{\rm ax} = 3.6$ m (1 T) (gray). The time resolution is 16 μs per frame as mentioned in Sec. 2. The data plotted are the average of the values at the same timing of all the discharges in the same group, and the error bar indicates their standard deviation. The values of $I_{\rm H_\alpha}(0)$ are normalized by its integral over the time period displayed in Fig. 5.

The horizontal axis, $t_{\rm rel}$, denotes the time relative to the timing at the maximum $I_{\rm H_\alpha}(0)$. Although the data acquisition is started by the trigger signal at the pellet injection, the actual timing of the signal detection in the observable time window of 4 ms is randomly shifted shot by shot. Therefore, $t_{\rm rel}$ has been adjusted in advance for each discharge such that the maximum $I_{\rm H_\alpha}(0)$ takes place at $t_{\rm rel} = 0$ μs. It is readily noticed in Fig. 5 (a) that the temporal development of $I_{\rm H_\alpha}(0)$ for $R_{\rm ax} = 3.6$ m (1 T) is almost identical to that for $R_{\rm ax} = 3.6$ m.

We have carried out least-squares fittings with the model spectrum described in Sec. 3 for the spectra taken at all the timings of all the discharges. Figures 5 (b), (c), and (d) show $T_{\rm e}$, $n_{\rm e}$, and V obtained as the result of the fittings. The values plotted are again the average of the results at the same timing of all the discharges in the same group, and their standard deviations are given as the error bars.

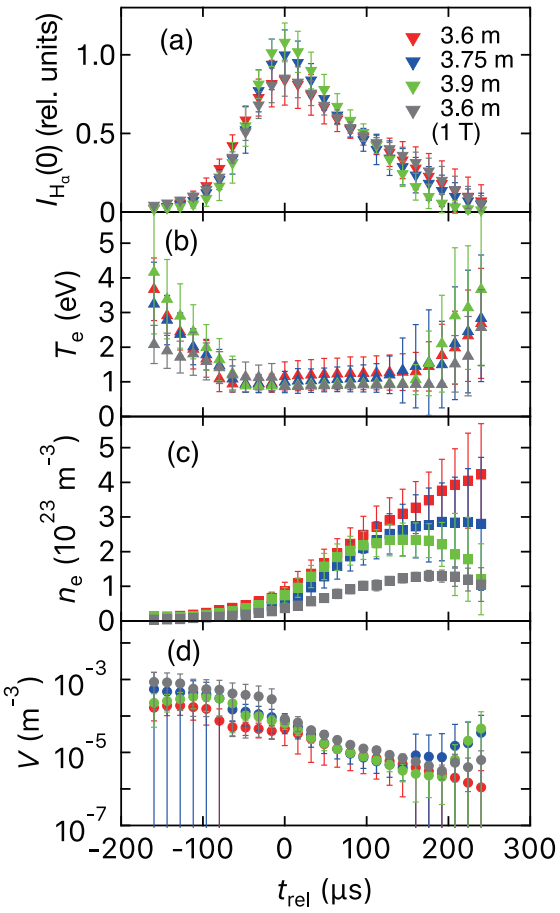

Fig. 5 Intensity of the Balmer-α line center (a) and parameters obtained in fittings of the measured spectra; (b) T_e, (c) n_e, and (d) V. The red, blue, and green symbols correspond to R_{ax} = 3.6 m, 3.75 m, and 3.9 m, respectively. The gray symbols show the results for R_{ax} = 3.6 m but with a low magnetic field strength (1 T). The errors are the standard deviation evaluated from all the spectra in each R_{ax} group used for the analysis. The dashed lines show the results of the least-squares fittings.

In both the R_{ax} = 3.6 m and R_{ax} = 3.6 m (1 T) cases, T_e first takes several electronvolts and decreases down to approximately 1 eV with increasing $I_{H_\alpha}(0)$, and then keeps to be almost unchanged for a certain period. After $I_{H_\alpha}(0)$ takes the maximum, T_e starts to increase up to values similar to those at the beginning while $I_{H_\alpha}(0)$ decreases. On the other hand, n_e is found to remain increasing even after $I_{H_\alpha}(0)$ takes the maximum.

It is found that n_e for R_{ax} = 3.6 m (1 T) is significantly lower than that for R_{ax} = 3.6 m at all times. Intuitively, this result is understandable because in the low magnetic field case, it is expected that the confinement in the ablation cloud is worse so that the plasma is swelled in the direction perpendicular to the magnetic field lines. As a result, n_e is lowered. The plasma volume V for R_{ax} = 3.6 m (1 T) actually appears slightly larger than that for R_{ax} = 3.6 m. For a quantitative understanding of the present results, however, the assistance of simulation studies of the pellet ablation phenomena would be necessary.

It is here noted that a sudden decrease is observed in T_e and V at around t_{rel} = 0 μs especially for R_{ax} = 3.6 m (1 T). This change seems to be caused by small but significant increase in the radiative attachment continuum which leads to lowering of T_e in the fitting. When T_e is lowered, excited level populations relative to n_i become larger as expected from Eq. (1), and then V is decreased as compensation.

We have also made measurements for discharges with different magnetic axis positions, i.e., R_{ax} = 3.6 m, 3.75 m, and 3.9 m. The maximum magnetic field strength is adopted for each R_{ax}, i.e., B_{ax} = 2.75 T, 2.64 T, and 2.54 T for R_{ax} = 3.6 m, 3.75 m, and 3.9 m, respectively. The R_{ax} = 3.75 m and 3.9 m groups consist of 21 and 13 discharges, respectively, and the R_{ax} = 3.6 m group is the same as that used for investigating the B_{ax} dependence.

The values of $I_{H_\alpha}(0)$ and the fitting results are plotted in Fig. 5 with blue symbols for R_{ax} = 3.75 m and green symbols for R_{ax} = 3.9 m. It is found that the peak width of $I_{H_\alpha}(0)$ in Fig. 5 (a) becomes narrower when R_{ax} is shifted outward, which indicates that the ablation is completed more quickly for larger R_{ax} cases. No clear difference is found in T_e derived in the fittings among the three R_{ax} cases. At the final stage of the ablation process, n_e appears to behave differently depending on R_{ax}. However, no definitive statement can be made due to their large uncertainties.

In conclusion, it has been found for the first time that n_e in the ablation cloud depends on the magnetic field strength while T_e shows no significant dependence, and that the ablation takes a longer time when R_{ax} is inward shifted. These results suggest a relationship concerning the plasma confinement characteristics between in the ablation cloud and in the background plasma. Although detailed mechanisms which determine the plasma parameters in the pellet ablation cloud remain open, the present results should have noticeable significance in the pellet ablation study for the fusion plasma.

Acknowledgments

We are grateful to all members of the LHD experiment group for their help in accomplishing the discharges and the measurements. This work is partly supported by JSPS KAKENHI Grant Number 18K03588 and by the National Institute for Fusion Science grant administrative budgets (ULHH028).

[1] S.S. Milora, W.A. Houlberg, L.L. Lengyel and V. Mertens, Nucl. Fusion **35**, 657 (1995).
[2] M. Goto, R. Sakamoto and S. Morita, Plasma Phys. Control. Fusion **49**, 1163 (2007).
[3] G. Motojima, R. Sakamoto, M. Goto *et al.*, Rev. Sci. Instrum. **83**, 093506 (2012).
[4] G. Seguineaud, G. Motojima, Y. Narushima and M. Goto, Atoms **6**, 34 (2018).

[5] R. Sakamoto, H. Yamada, K. Tanaka *et al.*, Nucl. Fusion **41**, 381 (2001).
[6] T. Fujimoto, *Plasma Spectroscopy* (Oxford University Press, Oxford, 2004).
[7] C. Stehlé and R. Hutcheon, Astron. Astrophys. **140**, 93 (1999).
[8] P.J. Storey and D.G. Hummer, Comput. Phys. Commun. **66**, 129 (1991).
[9] A.W. Wishart, Mon. Not. R. Astron. Soc. **187**, 59 (1979).
[10] D.R. Inglis and E. Teller, Astrophys. J. **90**, 439 (1939).